

Article

# Iridium-Based Nanohybrids: Synthesis, Characterization, Optical Limiting, and Nonlinear Optical Properties

Nikolaos Chazapis<sup>1,2</sup>, Michalis Stavrou<sup>1,2</sup>, Georgia Papaparaskaeva<sup>3</sup> , Alexander Bunge<sup>4</sup>, Rodica Turcu<sup>4</sup> ,  
Theodora Krasia-Christoforou<sup>3,\*</sup> and Stelios Couris<sup>1,2,\*</sup> 

<sup>1</sup> Department of Physics, University of Patras, 26504 Patras, Greece; n.chazapis@iceht.forth.gr (N.C.); m.stavrou@iceht.forth.gr (M.S.)

<sup>2</sup> Institute of Chemical Engineering Sciences (ICE-HT), Foundation for Research and Technology-Hellas (FORTH), 26504 Patras, Greece

<sup>3</sup> Department of Mechanical and Manufacturing Engineering, University of Cyprus, 1 Panepistimiou Avenue, Aglantzia, Nicosia 2109, Cyprus; papaparaskaeva.georgia@ucy.ac.cy

<sup>4</sup> National Institute R&D of Isotopic and Molecular Technologies, 400293 Cluj-Napoca, Romania; alexander.bunge@itim-cj.ro (A.B.); rodica.turcu@itim-cj.ro (R.T.)

\* Correspondence: krasia.theodora@ucy.ac.cy (T.K.-C.); couris@upatras.gr (S.C.)

**Abstract:** The present work reports on the synthesis and characterization of iridium (Ir)-based nanohybrids with variable chemical compositions. More specifically, highly stable polyvinylpyrrolidone (PVP) nanohybrids of the PVP-IrO<sub>2</sub> and PVP-Ir/IrO<sub>2</sub> types, as well as non-coated Ir/IrO<sub>2</sub> nanoparticles, are synthesized using different synthetic protocols and characterized in terms of their chemical composition and morphology via X-ray photoelectron spectroscopy (XPS) and scanning transmission electron microscopy (STEM), respectively. Furthermore, their nonlinear optical (NLO) response and optical limiting (OL) efficiency are studied by means of the Z-scan technique, employing 4 ns laser pulses at 532 and 1064 nm. The results demonstrate that the PVP-Ir/IrO<sub>2</sub> and Ir/IrO<sub>2</sub> systems exhibit exceptional OL performance, while PVP-IrO<sub>2</sub> presents very strong saturable absorption (SA) behavior, indicating that the present Ir-based nanohybrids could be strong competitors to other nanostructured materials for photonic and optoelectronic applications. In addition, the findings denote that the variation in the content of IrO<sub>2</sub> nanoparticles by using different synthetic pathways significantly affects the NLO response of the studied Ir-based nanohybrids, suggesting that the choice of the appropriate synthetic method could lead to tailor-made NLO properties for specific applications in photonics and optoelectronics.

**Keywords:** Ir nanoparticles; IrO<sub>2</sub> nanoparticles; colloidal nanohybrids; z-scan; nonlinear optical response



**Citation:** Chazapis, N.; Stavrou, M.; Papaparaskaeva, G.; Bunge, A.; Turcu, R.; Krasia-Christoforou, T.; Couris, S. Iridium-Based Nanohybrids: Synthesis, Characterization, Optical Limiting, and Nonlinear Optical Properties. *Nanomaterials* **2023**, *13*, 2131. <https://doi.org/10.3390/nano13142131>

Academic Editors: Zhiping Luo, Navadeep Shrivastava and Gibin George

Received: 30 June 2023  
Revised: 14 July 2023  
Accepted: 20 July 2023  
Published: 22 July 2023



**Copyright:** © 2023 by the authors. Licensee MDPI, Basel, Switzerland. This article is an open access article distributed under the terms and conditions of the Creative Commons Attribution (CC BY) license (<https://creativecommons.org/licenses/by/4.0/>).

## 1. Introduction

Nanomaterials based on precious metals such as palladium (Pd), platinum (Pt), gold (Au), silver (Ag), rhodium (Rh), ruthenium (Ru) and iridium (Ir) have attracted great attention in recent years due to their unique optical, catalytic and electronic properties. Consequently, such nanomaterials are extensively explored in many diverse areas including catalysis [1–3], sensing and biosensing [4,5], biomedicine [6,7], wastewater treatment [8] and optoelectronics [9,10].

From the aforementioned precious nanomaterials, not as much work has been reported on Ir-based nanosystems compared to other types of precious metals. The fact that Ir-based nanomaterials are usually characterized by extremely small nanoparticle/cluster diameters makes their characterization quite challenging [11]. Moreover, there is still a knowledge gap in respect to their formation mechanism governing their morphological characteristics and chemical composition [12,13].

Various synthetic approaches have been employed in the preparation of Ir-based nanomaterials [14]. These include chemical, photochemical and electrochemical reduction

processes; thermal decomposition; and hydrothermal, sonochemical microwave-assisted synthetic strategies. In most of these synthetic routes, stabilization was accomplished in the presence of polymers and surfactants [15,16], whereas surfactant-free stabilization was also proven to be highly effective, enabling the generation of stable Ir-based nanocolloids [17,18]. Among others, it has been demonstrated that such stabilizing mechanisms may enhance the activity of Ir-based nanomaterials by preventing their agglomeration, while retaining their chemical characteristics [19].

Based on the above, it becomes obvious that the scientific community has been highly active with regard to the development of Ir-based nanosystems since the latter are considered to be extremely promising in many applications [11], including electrochemical water splitting [20], wastewater treatment [21], sensing and biosensing [22], biomedicine [23] and optics [24].

The large optical nonlinearities of metal and semiconducting nanoparticles are undoubtedly a key advantage for their implementation in photonic devices [25–38]. To date, immense research efforts have been devoted to the investigation of the exceptional saturable absorption (SA) properties (nonlinear absorption coefficient  $\beta$ , modulation depth  $\alpha_s$  and saturable intensity  $I_s$ ) of low-dimensional nanostructures under ns laser radiation, demonstrating their great prospects for the generation of short laser pulses in Q-switched laser systems [25–32]. Other published research articles, primarily focused on the nonlinear optical (NLO) absorption of semiconducting nanoparticles, have revealed their high optical limiting (OL) efficiency [33–38]. Thus, they could be used for OL-related applications, such as the protection of human retinal and sensitive optical devices from an intense laser beam and in several technologically important fields, ranging from medical applications, optical imaging and telecommunications to laser material processing and defense systems [39–42]. Although numerous studies have appeared so far discussing the NLO response (NLO absorption and refraction) [25–32,43–45] and OL efficiency [33–38] of various metal and semiconducting nanoparticles, to the best of our knowledge, related studies on Ir-based nanohybrids are rather scarce, narrowing their practical application in photonics and optoelectronics.

In that context, solutions of Ir-based nanocolloids, namely polyvinylpyrrolidone-stabilized IrO<sub>2</sub> nanoparticles (PVP-IrO<sub>2</sub>), a mixture of PVP-stabilized Ir/IrO<sub>2</sub> nanoparticles with an Ir/IrO<sub>2</sub> ratio of ~0.25 (PVP-Ir/IrO<sub>2</sub>) and a mixture of Ir/IrO<sub>2</sub> nanoparticles without polymeric coating and an Ir/IrO<sub>2</sub> ratio of ~1 (Ir/IrO<sub>2</sub>), were generated by following three different synthetic protocols. PVP was used as a macromolecular steric stabilizer due to its non-toxicity, low cost and high effectiveness in acting as a stabilizing agent for numerous types of inorganic nanomaterials [46]. Furthermore, based on a previous study, it has been demonstrated that PVP-stabilized Ir NPs generated in methanol were characterized by very small diameters while retaining excellent stability in solution for several months [15]. The aforementioned Ir-based nanocolloids were further characterized in respect to their NLO response and OL performances using 4 ns laser pulses at 532 and 1064 nm.

## 2. Materials and Methods

### 2.1. Materials

Iridium (III) chloride hydrate (IrCl<sub>3</sub>·3H<sub>2</sub>O; Mw = 298.58 gmol<sup>-1</sup>, anhydrous basis, 99.9% trace metal basis) and polyvinylpyrrolidone (PVP; average Mw = 1,300,000 gmol<sup>-1</sup>) were purchased from Sigma-Aldrich Chemie GmbH, Taufkirchen, Germany. Sodium hydroxide (NaOH; Mw = 40.00 gmol<sup>-1</sup>) and methanol (MeOH; analytical grade) were purchased from Sigma-Aldrich Chemie GmbH, Taufkirchen, Germany and Sharlau Chemicals (Barcelona, Spain), respectively. All chemicals were used as received from the manufacturer without further purification. The Millex<sup>®</sup>-HP 13 mm filter unit (PES 0.45 μm membrane) that was employed in solution filtration was purchased from Sigma-Aldrich Chemie GmbH, Taufkirchen, Germany.

## 2.2. Synthesis of Ir-Based NP Solutions

Ir-based NP solutions were prepared in methanol, following 3 different experimental protocols (denoted as I, II and III, Figure 1), as described below.

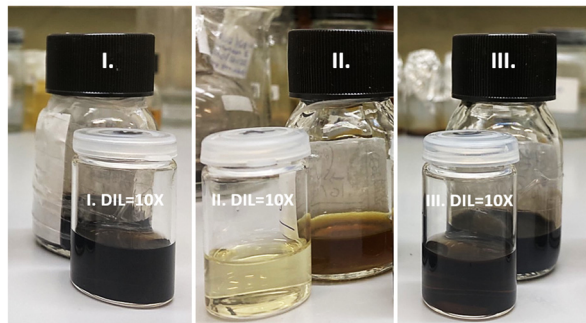


**Figure 1.** Highly stabilized Ir-based NP methanol solutions prepared by following 3 different synthetic protocols: (I) Ir/IrO<sub>2</sub>; (II) PVP-IrO<sub>2</sub>; and (III) PVP-Ir/IrO<sub>2</sub>.

(I) (Ir/IrO<sub>2</sub>) A dispersion of IrCl<sub>3</sub>·3H<sub>2</sub>O (134 mg, 0.45 mmol) was prepared in methanol (5 mL) via vigorous stirring (1250 rpm) for 1 h at room temperature. NaOH (153 mg, 765 mM) dissolved in methanol (5 mL) was then added dropwise (1 mL/min) into the IrCl<sub>3</sub>·3H<sub>2</sub>O/methanol dispersion under stirring conditions (500 rpm). The latter was left to stir for additional 2 h under reflux (65 °C) upon stirring (500 rpm), resulting in a clear, black-colored suspension (Figure 1). This was filtered (using PES 0.45 μm membrane syringe filters), and its color remained stable, while no precipitation phenomena were observed.

(II) (PVP-IrO<sub>2</sub>) PVP (1 g, 9 mmol of vinylpyrrolidone unit, 5 mL) was placed in a 50 mL round-bottom flask, and methanol (5 mL) was added. The resulting mixture was left to stir (500 rpm) for 10 min at room temperature, resulting in a clear, transparent polymer solution. In the meantime, a dispersion of IrCl<sub>3</sub>·3H<sub>2</sub>O (134 mg, 0.45 mmol) was prepared in methanol (5 mL) via vigorous stirring (1250 rpm) for 1 h at room temperature. The latter was added dropwise (1 mL/min) into the methanol solution containing PVP, followed by overnight stirring (500 rpm) at room temperature. The obtained solution was further stirred (500 rpm) for 6 h under reflux at 65 °C to yield a clear, bronze-colored suspension (Figure 1). This was filtered (using PES 0.45 μm membrane syringe filters), and its color remained stable, while no precipitation phenomena were observed.

(III) (PVP-Ir/IrO<sub>2</sub>) PVP (1 g, 9 mmol of vinylpyrrolidone unit, 5 mL) was placed in a 50 mL round-bottom flask and dissolved in a NaOH/methanol solution (153 mg, 765 mM, 5 mL). The resulting mixture was left to stir (500 rpm) for 10 min at room temperature, resulting in a clear, transparent polymer solution. In the meantime, a dispersion of IrCl<sub>3</sub>·3H<sub>2</sub>O (134 mg, 0.45 mmol) was prepared in methanol (5 mL) via vigorous stirring (1250 rpm) for 1 h at room temperature. The latter was added dropwise (1 mL/min) into the NaOH/methanol solution containing PVP, followed by overnight stirring (500 rpm) at room temperature. The obtained solution was further stirred (500 rpm) for 6 h under reflux at 65 °C, resulting in a clear, black-colored suspension (Figure 1). This was filtered (using PES 0.45 μm membrane syringe filters), and its color remained stable, while no precipitation phenomena were observed.

All the above-described Ir-based systems were subjected to 10× dilution prior to their characterization.

## 2.3. Materials Characterization

The surface chemical composition of the samples was investigated by X-ray photoelectron spectroscopy (XPS) using an XPS spectrometer SPECS equipped with a dual-anode X-ray source Al/Mg, a PHOIBOS 150 2D CCD hemispherical energy analyzer and a multi-channeltron detector with vacuum pressure maintained at  $1 \times 10^{-9}$  torr. The particle

suspension was dried on an indium foil prior to the XPS measurements. Data analysis and curve fitting were performed using CasaXPS software.

The size and shape of the Ir-based nanostructures were examined by scanning transmission electron microscopy (STEM) with a Hitachi HD2700 equipped with a cold field emission gun, Dual EDX System (X-Max N100TLE Silicon Drift Detector (SDD)) from Oxford Instruments. For the analysis, the methanolic suspension of Ir-based nanoparticles was first dried, and the sample was resuspended in water. The nanoparticles were then centrifuged in an ultracentrifuge for several hours before being resuspended in water. The centrifugation was repeated again, and a suspension of the samples was sonicated (<10 s) with a UP100H ultrasound finger and deposited using the droplet method on a 400-mesh copper grid coated with a thin carbon layer. For both types of analysis, the nominal operating tension was 200 kV. The size of the nanoparticles was determined using the ImageJ software.

#### 2.4. Z-Scan Measurements

The third-order nonlinear optical (NLO) response of the studied Ir-based nanohybrids was investigated by means of the conventional single-beam Z-scan technique. Further information on this technique and the procedures followed for the analysis of the obtained data are reported in detail elsewhere [47], and only a short description is given herein. The Z-scan technique simultaneously provides information about the sign and the magnitude of the NLO absorption and refraction of a sample, which can be expressed in terms of the nonlinear absorption coefficient  $\beta$  and nonlinear refractive index parameter  $\gamma'$ , respectively. These NLO quantities can be determined by measuring the variation in the sample's normalized transmittance, as it is driven by a stepper motor along the propagation direction (e.g., the z-axis) of a focus laser beam, by means of two different experimental configurations, the so-called "open aperture" (OA) and "closed aperture" (CA) Z-scans. In the former configuration (i.e., the OA Z-scan), the transmitted laser beam is totally collected by a lens and measured by a detector (e.g., a photomultiplier (PMT)), allowing for the determination of the nonlinear absorption coefficient  $\beta$ . Simultaneously, in the latter configuration (i.e., the CA Z-scan), where only a part of the transmitted laser beam is measured by a second PMT after it has passed through a narrow pinhole positioned in the far field, information about the nonlinear refraction of the sample (i.e., the nonlinear refractive index parameter  $\gamma'$ ) is provided.

In general, the presence of a transmission maximum/minimum in the OA Z-scan reveals saturable absorption (SA)/reverse saturable absorption (RSA) behavior of the sample, corresponding to a negative/positive nonlinear absorption coefficient  $\beta$ . Similarly, the presence of a pre-focal transmission minimum followed by a post-focal maximum or vice versa in the CA Z-scan denotes a self-focusing ( $\gamma' > 0$ ) or self-defocusing ( $\gamma' < 0$ ) behavior, respectively. It is interesting to note that the CA Z-scan measurements can be also affected by the NLO absorption of the sample. In this case, the CA Z-scan recordings are asymmetric with respect to the focal plane. Thus, in order to remove the contribution of NLO absorption on the CA Z-scan recording, the latter is divided by the corresponding OA Z-scan, providing the so-called "divided" Z-scan recording, which is used for the direct determination of the nonlinear refractive index parameter  $\gamma'$ .

The values of  $\beta$  and  $\gamma'$  are calculated by fitting the experimental OA and "Divided" Z-scans with Equations (1) and (2), respectively:

$$T(x) = \frac{1}{\sqrt{\pi} \left( \frac{\beta I_0 L_{\text{eff}}}{1+x^2} \right)} \int_{-\infty}^{+\infty} \ln \left[ 1 + \frac{\beta I_0 L_{\text{eff}}}{1+(x)^2} e^{-t^2} \right] dt \quad (1)$$

$$T(x) = 1 - \frac{4\gamma' k I_0 L_{\text{eff}} x}{(1+x^2)(9+x^2)} \quad (2)$$

where  $x = z/z_0$  with  $z$  and  $z_0$  denoting the sample's position and Rayleigh length, respectively,  $I_0$  is the on-axis peak irradiance,  $L_{\text{eff}}$  is the sample's effective length and  $k$  is the wavenumber at the excitation wavelength.

Using the determined values of  $\beta$  and  $\gamma'$ , the real and the imaginary parts of the third-order susceptibility  $\chi^{(3)}$  can be deduced through Equations (3) and (4), respectively:

$$\text{Im}\chi^{(3)}(\text{esu}) = 10^{-7} \frac{c^2 n_0^2 \beta}{96\pi^2 \omega} \quad (3)$$

$$\text{Re}\chi^{(3)}(\text{esu}) = 10^{-6} \frac{c n_0^2 \gamma'}{480\pi^2} \quad (4)$$

where  $c$  is the speed of light,  $n_0$  is the refractive index and  $\omega$  is the frequency of the incident laser beam. To facilitate comparisons among samples having different linear absorption  $\alpha_0$ , the determined NLO parameters (i.e., imaginary/real parts of the third-order nonlinear susceptibility  $\chi^{(3)}$ ) are divided by the respective absorption  $\alpha_0$ , providing a figure of merit (FOM) for these quantities.

The laser source used for the Z-scan experiments was a Q-switched Nd:YAG laser system (EKSPLA NT 342/3/UVF/AW), delivering 4 ns laser pulses at 1064 (fundamental frequency) and 532 nm (SHG) with a variable repetition rate from 1 to 10 Hz. For the Z-scan measurements, two different concentrations of the studied Ir-based colloidal solutions in methanol (i.e., 0.5 and 1%  $w/v$ ) were prepared and placed into 1 mm path length quartz cells. The laser beam was focused into the samples by means of a 20 cm focal length quartz lens. The laser beam radii at the focal plane were measured using a CCD camera and found to be about  $(18 \pm 2)$  and  $(30 \pm 2)$   $\mu\text{m}$  for the 532 and 1064 nm laser outputs, respectively.

### 2.5. Optical Limiting

To assess the optical limiting (OL) performance of the studied Ir-based nanohybrids, under 4 ns 532 nm laser irradiation, the OA Z-scan recordings were used to plot the variation in the sample's transmittance as a function of the input laser fluence  $F_{\text{in}}(z)$ . For the calculation of the values of  $F_{\text{in}}(z)$  at each  $z$ -position, the following equation was used:

$$F_{\text{in}}(z) = \frac{4\sqrt{\ln 2} E_{\text{in}}}{\pi^{3/2} r(z)^2} \quad (5)$$

where  $E_{\text{in}}$  is the incident laser energy and  $r(z)$  is the beam radius at each  $z$ -position, the latter given by the relation:

$$r(z) = r(0) \left[ 1 + (z/z_0)^2 \right]^{\frac{1}{2}} \quad (6)$$

To check for possible contribution of nonlinear scattering (NLS) signal to the OL performance of the samples, a high-precision photodiode was used, which was placed on a goniometric stage, monitoring the scattered laser radiation at different angles with respect to the laser propagation. However, within the range of incident laser intensities used for the Z-scan measurements, no significant NLS signal was detected, indicating a rather negligible contribution of NLS to the OL performance of the studied Ir-based nanohybrids.

## 3. Results and Discussion

### 3.1. Chemical Composition and Morphology

STEM was performed on samples I–III (Figure 2). For sample I (Ir/IrO<sub>2</sub>), the nanoparticles could only be seen clustered into larger agglomerates overlapping each other (see also Figure S2 in Supporting Information), unlike sample III (PVP-Ir/IrO<sub>2</sub>), where at least parts of the sample were found in almost perfect monolayers. The individual nanoparticles were uniform and monodisperse, with an average diameter of  $1.6 \pm 0.28$  nm. The presence of Ir in EDX (Figure 3) confirmed that Ir-containing nanoparticles were generated in all three cases. In the electron micrographs of sample III (PVP-Ir/IrO<sub>2</sub>), the nanoparticles were much more spread out. The average diameter was slightly smaller, at  $1.4 \pm 0.24$  nm, and exhibited uniformity and good dispersity (i.e., fairly monodisperse). The comparatively smaller amount of iridium relative to the amount of carbon (with small contributions from

PVP and a large contribution from the carbon grid underground) visible in EDX stems from the fact that the nanoparticles are very small and arranged in a monolayer on the carbon grid. The decrease in tendency to agglomerate is likely due to the steric stabilization provided by PVP, which also resulted in a higher stability in suspension—even repeated washing after centrifugation could not completely remove the polymeric coating. In sample II (PVP-IrO<sub>2</sub>), the separation of nanoparticles by centrifugation was unsuccessful. As a result, the presence of a large amount of the polymer coating prevented the acquisition of clear images of the Ir-based nanoparticles, and hence the nanoparticles shown in Figure 2 (top) are indistinguishable. Nevertheless, the fact that this area does contain nanoparticles is proven by EDX, which clearly shows the presence of Ir, O and N (with the latter verifying the presence of PVP). The comparatively large ratio of Ir to C in EDX makes it likely that also in this case the nanoparticles are stacked in more than a monolayer, similar to sample I.

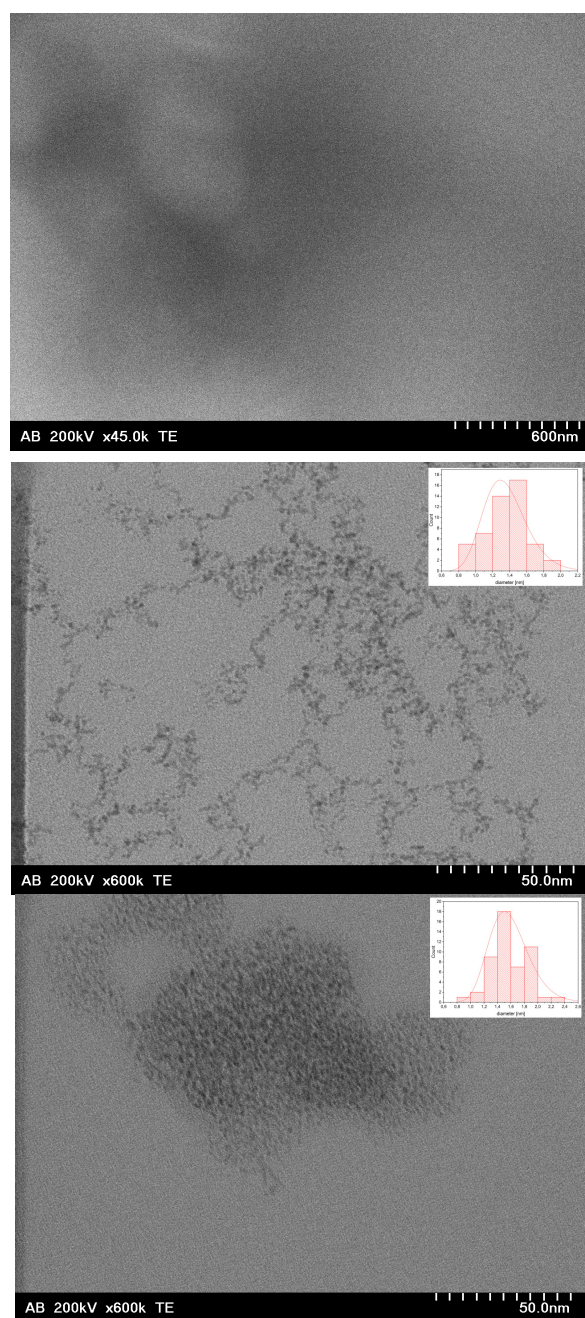


**Figure 2.** TEM of samples II (PVP-IrO<sub>2</sub>, **top**), III (PVP-Ir/IrO<sub>2</sub>, **middle**) and I (Ir/IrO<sub>2</sub>, **bottom**). Inset: size distributions for samples III and I.

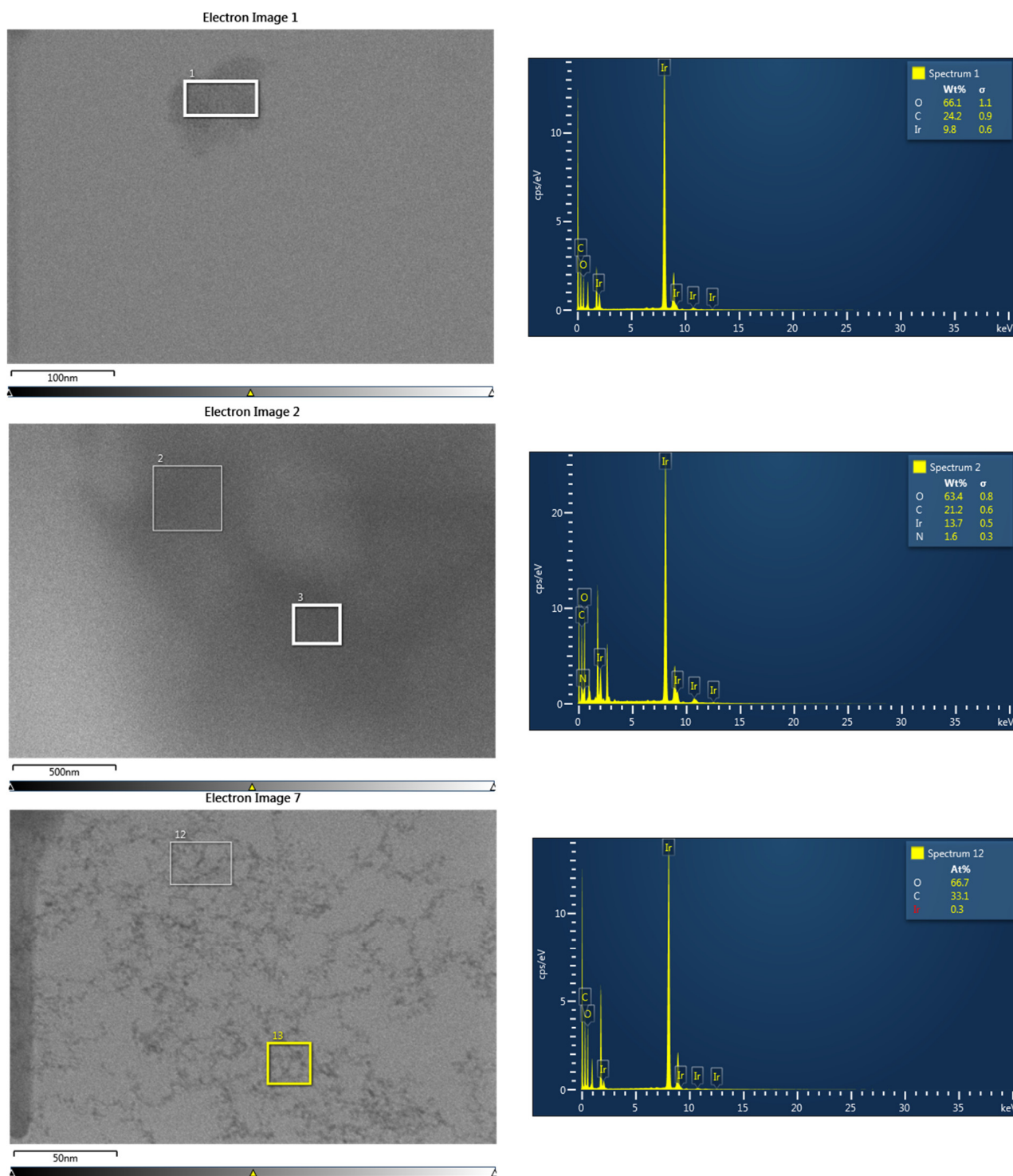


**Figure 3.** EDX of samples I (Ir/IrO<sub>2</sub>, **top**), II (PVP-IrO<sub>2</sub>, **middle**) and III (PVP-Ir/IrO<sub>2</sub>, **bottom**).

The XPS investigation of samples II (PVP-IrO<sub>2</sub>), III (PVP-Ir/IrO<sub>2</sub>) and I (Ir/IrO<sub>2</sub>) evidence differences in their chemical composition. The survey spectra for the three samples are given in Figure 4, while in Figures 5–7, the high-resolution XPS spectra of the elements for the above-mentioned systems are provided. As seen in Figure 4, the characteristic signal corresponding to nitrogen appears only in samples II and III as expected, since PVP is present only in those two samples.

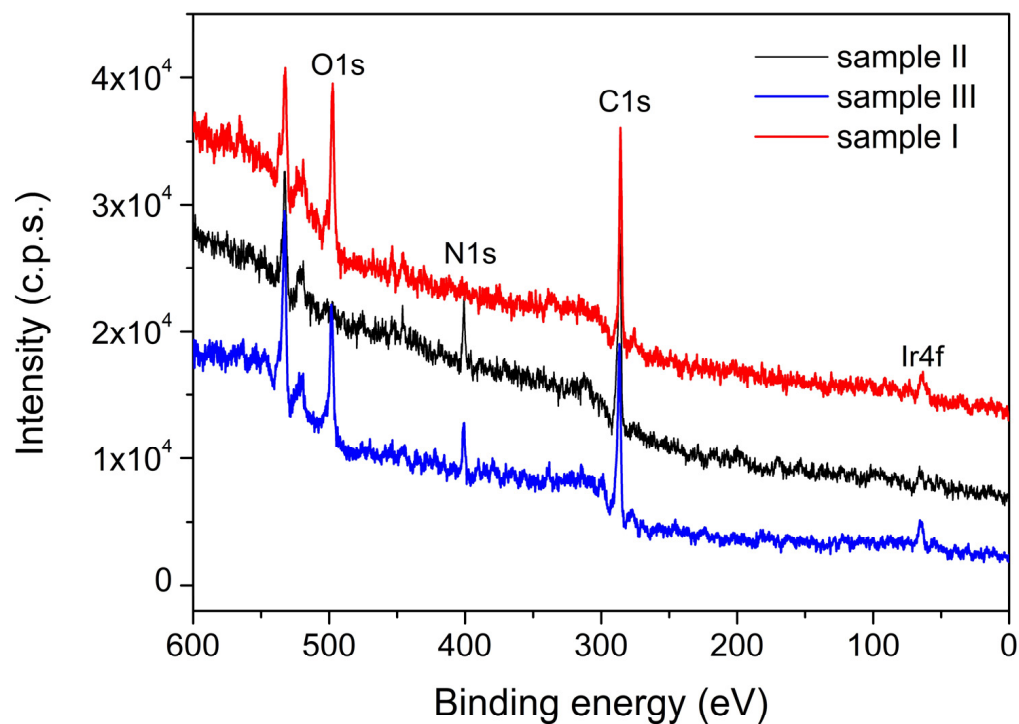


Figure 4. The XPS survey spectra for samples II (PVP-IrO<sub>2</sub>), III (PVP-Ir/IrO<sub>2</sub>) and I (Ir/IrO<sub>2</sub>).

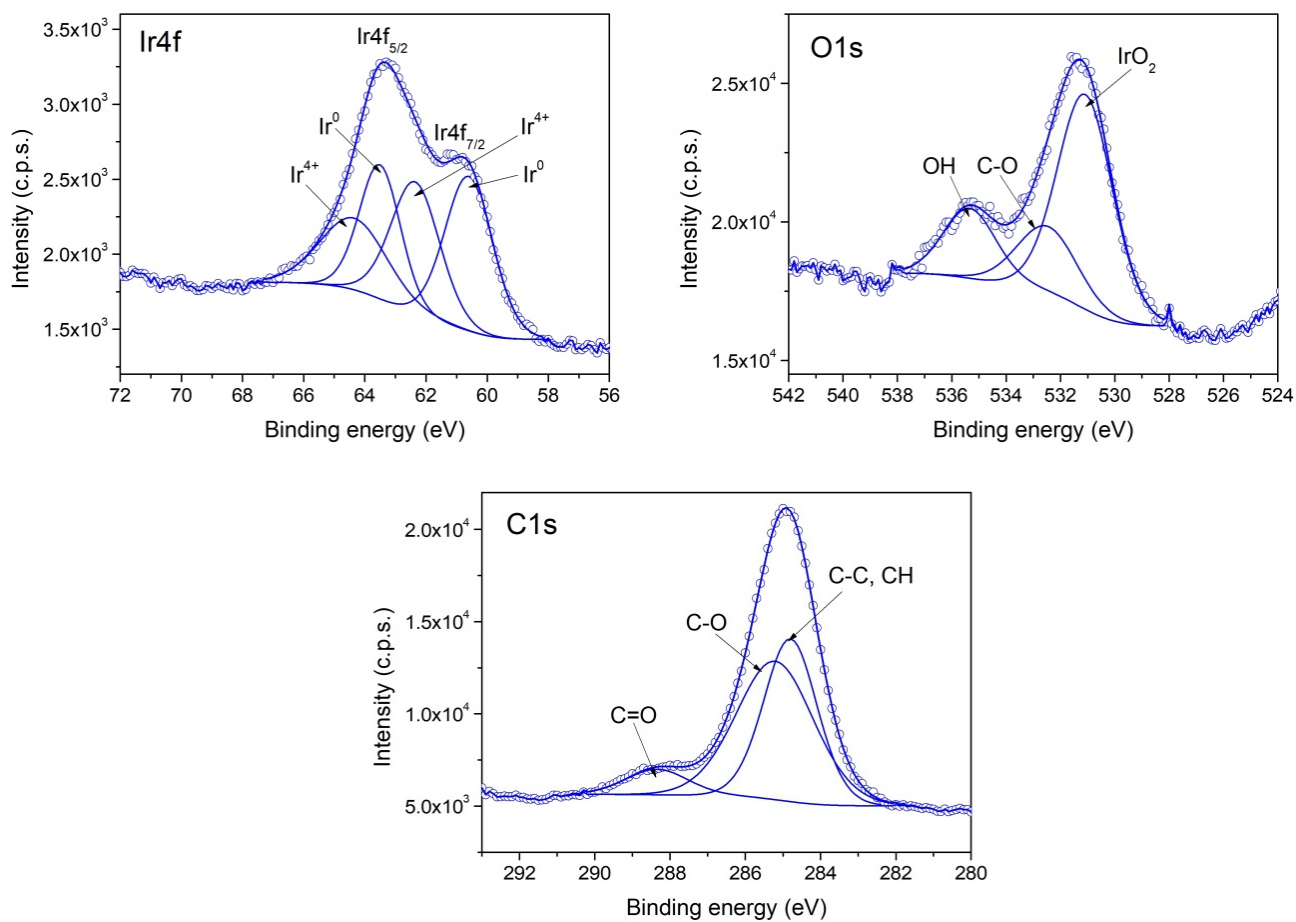
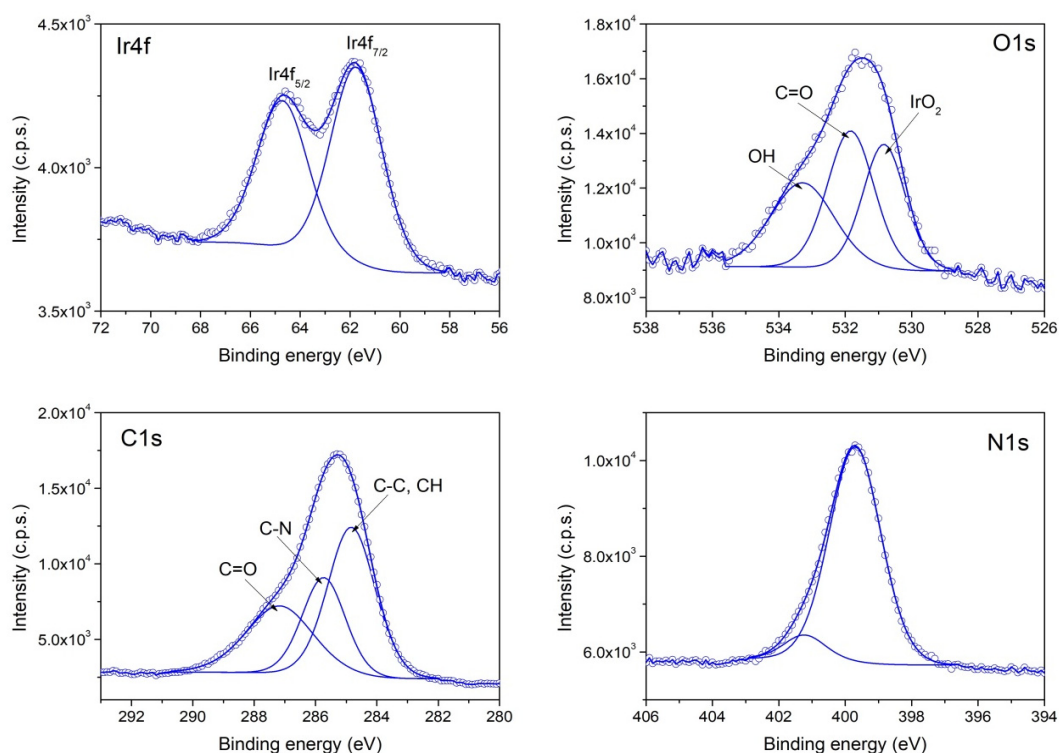
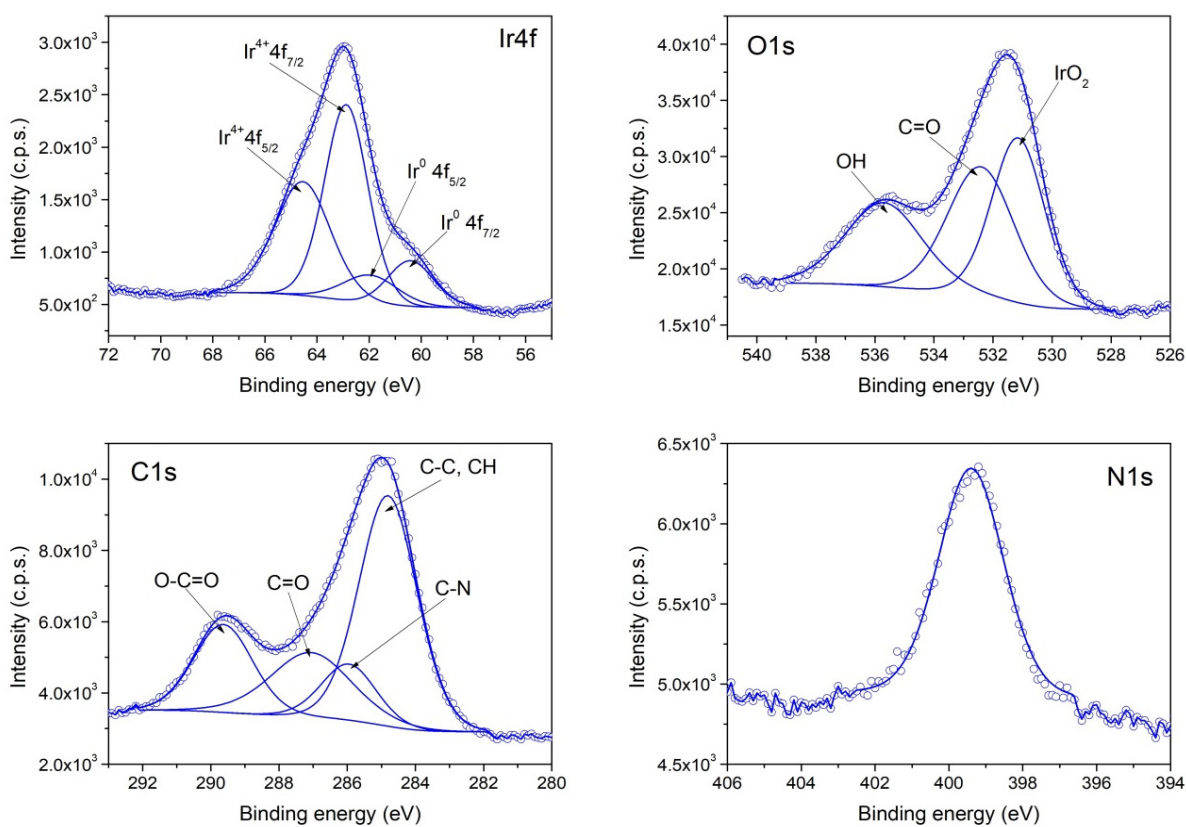


Figure 5. XPS spectra of Ir4f, O1s and C1s core levels from Sample I.



**Figure 6.** XPS spectra of Ir4f, O1s and C1s and N1s core levels from Sample II.



**Figure 7.** XPS spectra of Ir4f, O1s and C1s and N1s core levels from Sample III.

According to the XPS spectra appearing in Figure 6, sample II contains only  $\text{IrO}_2$ , because the Ir4f spectrum contains two components that have the corresponding binding energies for  $\text{Ir}^{4+}$ . In the case of sample III, the recorded Ir4f spectrum appearing in Figure 7

shows that  $\text{Ir}^0$  and  $\text{IrO}_2$  co-exist in an atomic concentration ratio  $\text{Ir}^0/\text{Ir}^{4+} = 0.25$ . Finally, in sample I (Figure 5), a mixture of  $\text{Ir}^0$  and  $\text{IrO}_2$  is also present, with an atomic concentration ratio:  $\text{Ir}^0/\text{Ir}^{4+} = 1$ .

### 3.2. NLO Properties

In Figure 8, representative UV-Vis-NIR absorption spectra of the prepared Ir-based nanohybrid solutions (PVP- $\text{IrO}_2$ —sample II; PVP-Ir/ $\text{IrO}_2$ —sample III; Ir/ $\text{IrO}_2$ —sample I) prepared in methanol (0.5% *w/v*) are presented. As shown, all the Ir-based nanohybrids exhibited an absorption maximum at 300 nm, ascribed to the Ir-monomer precursor [48], while the absorption spectrum of PVP- $\text{IrO}_2$  also displayed three shoulders at ~330, 380 nm and 540 nm. More specifically, the absorbance peaks of PVP- $\text{IrO}_2$  at ~330 and 380 nm are most likely attributed to the iridium (III) chloride salt [49], while the appearance of the absorbance peak at ~540 nm, ascribed to  $\text{Ir}^{3+}$  to  $\text{Ir}^{4+}$  transitions, is typical of  $\text{IrO}_2$  nanoparticles [50]. The UV-Vis-NIR absorption spectra shown in Figure S3, which have been taken for all samples in different periods, support the stability of the solutions. As can be seen from this figure, all the measured spectra did not present any change in the morphology and the absorbance values, confirming the high stability of the solutions over a long period of time.

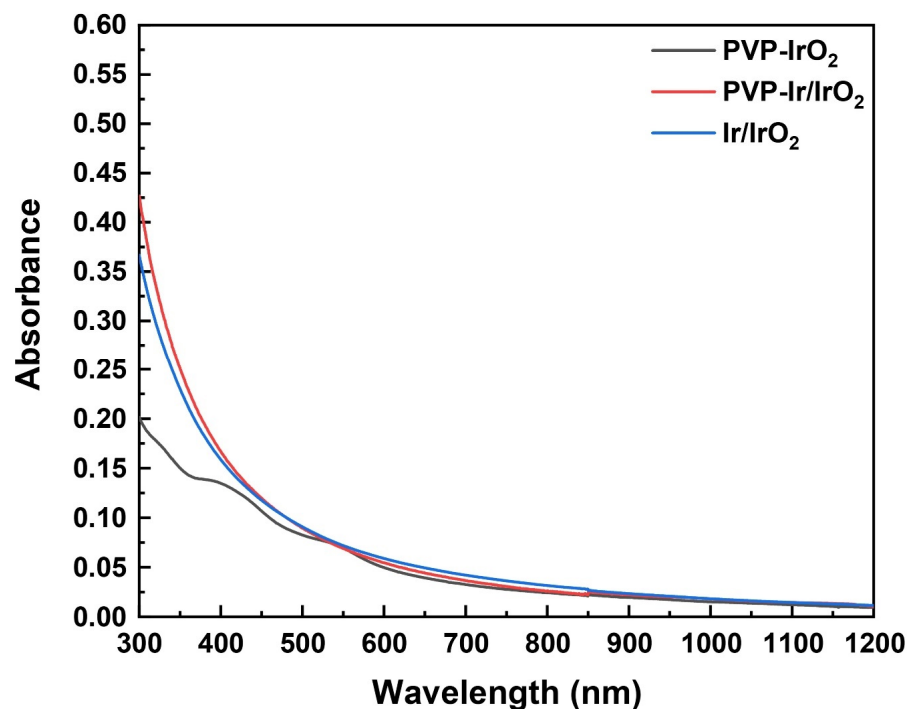


**Figure 8.** UV-Vis-NIR absorption spectra of Ir-based nanohybrids (all corresponding to a 0.5% *w/v* solution concentration).

In Figure 9a,c,e, representative OA Z-scans of the prepared Ir-based nanohybrid solutions, obtained under 4 ns 532 nm laser excitation using different laser intensities, are shown. To facilitate comparisons, all measured OA Z-scans correspond to solutions exhibiting the same linear absorption coefficient  $\alpha_0$ , i.e., of about  $1.8 \text{ cm}^{-1}$ , at 532 nm. The solid lines correspond to the best fits of the experimental data points (solid symbols) according to Equation (1). Similar OA Z-scan measurements performed under 4 ns 1064 nm laser excitation revealed insignificant NLO absorption for all samples. In addition, the possible contribution of the solvent (i.e., methanol) and polymer (i.e., PVP) to the NLO absorptive response of the solutions was checked and found to be insignificant within the range of laser intensities used (i.e., up to  $180 \text{ MW/cm}^2$ ) for the Z-scan measurements. Therefore, the presented OA Z-scans of Figure 9a,c,e provide the NLO absorptive response

of the Ir-based nanohybrids directly. As can be seen from Figure 9a, the OA Z-scans of PVP-IrO<sub>2</sub> revealed a maximum at the focal plane (i.e., at  $z = 0$ ), indicative of a typical saturable absorption (SA,  $\beta < 0$ ) behavior. In addition, this transmission maximum was found to increase with incident laser intensity, retaining, however, a clear transmission maximum even for the highest laser intensity used, implying that a one-photon absorption (1PA)-related nonlinearity occurs under 532 nm laser excitation. However, since the bandgap energy of the studied IrO<sub>2</sub> semiconducting nanoparticles, evaluated to be  $\sim 2.7$  eV (see in Figure S1, Supplementary Information), is larger than the corresponding excitation photon energy at 532 nm ( $\sim 2.33$  eV), the SA behavior of PVP-IrO<sub>2</sub> may be assisted by the existence of abundant defect states within the bandgap, generated from oxygen-deficient phases [51,52]. In particular, due to the presence of defect states, the energy bandgap of IrO<sub>2</sub> can be bridged by electrons absorbing photons with lower energy, leading to a progressive increase in the carriers accumulated in its conduction band. When the sample is close to the focal plane ( $z = 0$ ), where the laser intensity is sufficiently strong, the interband optical transitions become more efficient, resulting in the depletion of all the available states in the conduction band of IrO<sub>2</sub>. Consequently, any further excitation of electrons is blocked due to the Pauli exclusion principle, giving rise to the appearance of SA behavior ( $\beta < 0$ ). From the fitting of the OA Z-scans of PVP-IrO<sub>2</sub> presented in Figure 9a, the mean value of the nonlinear absorption coefficient  $\beta$  was determined to be  $(-115.6 \pm 18.0) \times 10^{-11}$  m/W.

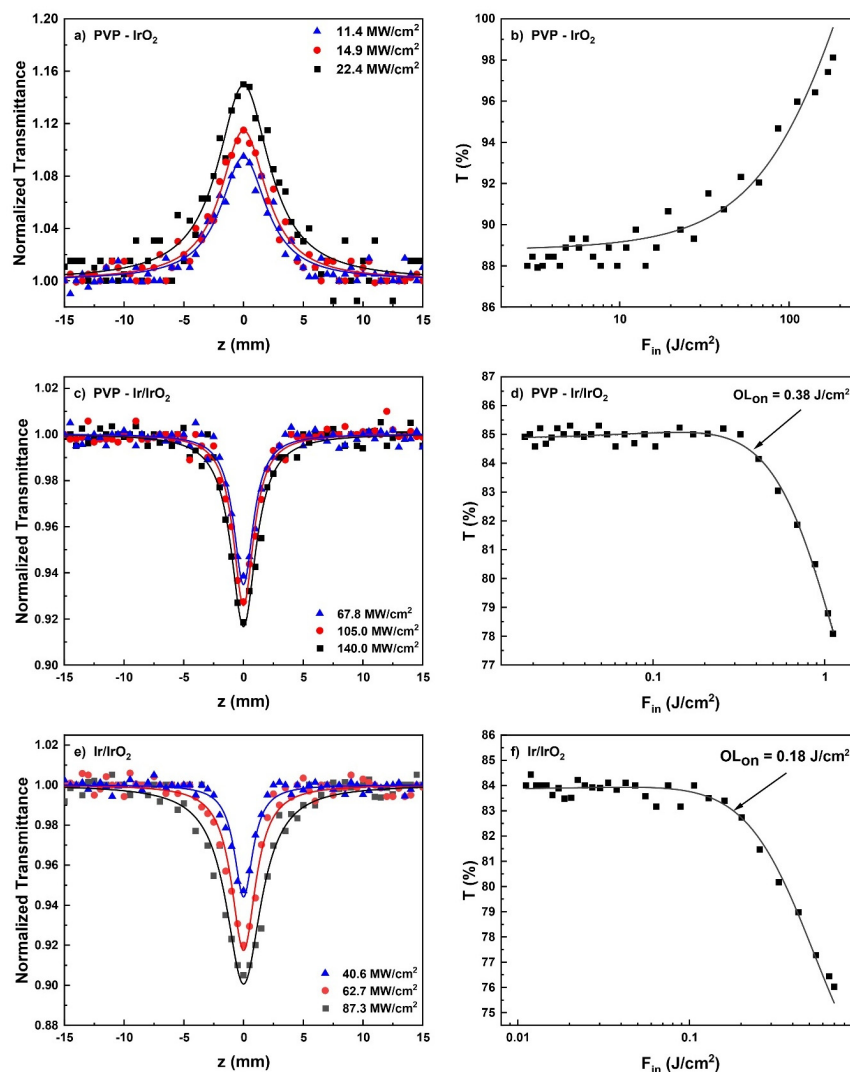


**Figure 9.** OA Z-scans (a,c,e) and variation in the transmittance (b,d,f) of PVP-IrO<sub>2</sub>, PVP-Ir/IrO<sub>2</sub>, Ir/IrO<sub>2</sub> nanohybrid solutions, under 4 ns, 532 nm laser excitation, using different laser excitation intensities.

Besides their large values of the nonlinear absorption coefficient  $\beta$ , materials suitable for saturable absorption applications are characterized by high modulation depth  $\alpha_s$  and low saturable intensity  $I_{\text{sat}}$ . For the determination of the  $\alpha_s$  and  $I_{\text{sat}}$  values of PVP-IrO<sub>2</sub>, the experimentally obtained values of normalized transmittance (solid points) have been plotted as a function of the incident laser intensity (see Figure 9b) and fitted using Equation (7):

$$T = 1 - \left( \frac{\alpha_s}{1 + I/I_{\text{sat}}} + \alpha_{\text{ns}} \right) \quad (7)$$

where  $\alpha_{\text{ns}}$  represents the non-saturable components. From the fitting of intensity-dependent transmittance, the values of  $\alpha_s$  and  $I_{\text{sat}}$  were determined to be ~4% and 80 MW/cm<sup>2</sup>, respectively. In order to highlight the efficiency of the PVP-IrO<sub>2</sub> system as a saturable absorber for the generation of laser pulses in Q-switched laser systems, its saturable absorption properties (i.e., the nonlinear absorption coefficient  $\beta$  (or  $\text{Im}\chi^{(3)}$ ), the modulation depth  $\alpha_s$  and the saturable intensity  $I_{\text{sat}}$ ) have been compared to those of other metal and semiconducting nanoparticles reported to exhibit exceptional SA response, including silver (Ag), gold (Au), platinum (Pt), palladium (Pd), zinc oxide (ZnO), vanadium pentoxide (V<sub>2</sub>O<sub>5</sub>), iron oxide ( $\gamma$ -Fe<sub>2</sub>O<sub>3</sub>), copper oxide (CuO) and copper hydroxide (Cu(OH)<sub>2</sub>) [25–32]. As presented in Table 1, the figure of merit of  $\text{Im}\chi^{(3)}$  (i.e., the quantity  $\text{Im}\chi^{(3)}/\alpha_0$ ) as well as the values of  $\alpha_s$  and  $I_{\text{sat}}$  of PVP-IrO<sub>2</sub> are comparable to those of other nanomaterials, emphasizing the efficiency of the studied IrO<sub>2</sub> nanoparticles for saturable absorption applications.

**Table 1.** Saturable absorption properties of PVP-IrO<sub>2</sub>, Ag, Au, Pt ZnO, V<sub>2</sub>O<sub>5</sub>, Pt,  $\gamma$ -Fe<sub>2</sub>O<sub>3</sub>, Cu(OH)<sub>2</sub>, Cu(OH)<sub>2</sub>/CuO and Pd nanoparticles.

Sample	Excitation Conditions	$\alpha_0$ (cm <sup>-1</sup> )	$\beta$ $\times 10^{-11}$ (m/W)	$\text{Im}\chi^{(3)}$ $\times 10^{-13}$ (esu)	$\text{Im}\chi^{(3)}/\alpha_0$ $\times 10^{-13}$ (esu cm)	$\alpha_s$ (%)	$I_{\text{sat}}$ (MW/cm <sup>2</sup> )	Ref.
PVP-IrO <sub>2</sub>	4 ns, 532 nm	1.77	-115.6	-53.0	-30.6	4	80	this work
Ag	7 ns, 532 nm	~9.2	-2562	-1178.0	128	N/A	32.1	[25]
Au	4 ns, 532 nm	~0.9	-17.6	-8.3	9.2	N/A	230	[26]
Pt	10 ns, 532 nm	0.91	-3	-8.53	9.4	N/A	18	[27]
Pd	4 ns, 532 nm	7.5	-54	-32.5	4.3	N/A	N/A	[28]
ZnO	1064 nm	6.8	-5.9	-6.7	0.99	N/A	N/A	[29]
V <sub>2</sub> O <sub>5</sub>	400 ns, 1560 nm	N/A	N/A	N/A	N/A	5	60	[29]
$\gamma$ -Fe <sub>2</sub> O <sub>3</sub>	0.7 ns, 1064 nm	N/A	N/A	N/A	N/A	21.8	0.33	[30]
	4 ns, 532 nm	~5.1	N/A	-2.2	0.43	N/A	N/A	[31]
	4 ns, 1064 nm	~1.15	N/A	-1.5	1.3	N/A	N/A	[31]
Cu(OH) <sub>2</sub>	4 ns, 532 nm	1	-97.3	-44.7	-44.7	N/A	N/A	[32]
Cu(OH) <sub>2</sub> /CuO	4 ns, 532 nm	1	-594	-273	-273	N/A	N/A	[32]

As shown in Figure 9c,e, the measured OA Z-scans of the solutions containing a mixture of Ir and IrO<sub>2</sub> nanoparticles, i.e., the PVP-Ir/IrO<sub>2</sub> and Ir/IrO<sub>2</sub> nanohybrid solutions, presented a deep focus, increasing with the laser pulse intensity, implying a positive absorptive nonlinearity (i.e., RSA behavior,  $\beta > 0$ ). From the fitting of these OA Z-scans with Equation (1), the average values of the nonlinear absorption coefficient  $\beta$  of PVP-Ir/IrO<sub>2</sub> and Ir/IrO<sub>2</sub> were determined to be  $(13.8 \pm 2.0) \times 10^{-11}$  and  $(24.2 \pm 2.0) \times 10^{-11}$  m/W, respectively, suggesting that the increase in the IrO<sub>2</sub> content leads to significant

enhancement of the NLO absorption of these nanohybrids. The same conclusion can also be drawn from the comparison of the  $\beta$  value of the PVP-IrO<sub>2</sub> solution, containing only IrO<sub>2</sub> nanoparticles, with the corresponding values of PVP-Ir/IrO<sub>2</sub> and Ir/IrO<sub>2</sub>. In particular, as mentioned above, the  $\beta$  value of PVP-IrO<sub>2</sub> was found to be  $(-115.6 \pm 18.0) \times 10^{-11}$  m/W, that is, ~5 and 10 times larger than those of Ir/IrO<sub>2</sub> and PVP-Ir/IrO<sub>2</sub>, respectively.

In general, the RSA behavior of the studied nanostructures can be explained in terms of different physical processes, such as excited state absorption (ESA), two-photon absorption (2PA), nonlinear scattering (NLS), and thermal cumulative effects [53]. The presence of NLS was investigated and found to be negligible under the present experimental conditions. In addition, any contribution arising from thermal effects should be excluded, as the laser repetition rate was set at as low as 1 Hz. Furthermore, trials using higher repetition rates (i.e., up to 10 Hz) did not show significant modifications of the sample's transmittance, ensuring the absence of such effects. Consequently, the NLO absorptive response of the present nanoparticles can be most likely attributed to ESA and/or 2PA processes. For a better understanding of the physical processes responsible for the NLO absorptive response of the PVP-Ir/IrO<sub>2</sub> and Ir/IrO<sub>2</sub> solutions, it should be considered that the optical bandgap of the IrO<sub>2</sub> semiconducting nanoparticles, estimated for the sample containing only IrO<sub>2</sub> nanoparticles (PVP-IrO<sub>2</sub>), is about 2.7 eV (see Figure S1, Supplementary Information) and that Ir nanoparticles exhibit zero bandgap energy. Therefore, since the bandgap of IrO<sub>2</sub> nanoparticles lies above the sum of energy of two photons at 532 nm (~2.33 eV), only 2PA can occur in IrO<sub>2</sub>. On the other hand, the zero bandgap of Ir nanoparticles facilitates the manifestation of ESA under 532 nm laser excitation. However, as discussed above, the irradiation of PVP-IrO<sub>2</sub> nanohybrids at 532 nm leads to SA behavior. As a result, it is reasonable to assume that the photo-response mechanism causing the NLO absorption of the present nanohybrids can be assigned to ESA due to the presence of Ir nanoparticles.

Materials exhibiting strong RSA behavior are promising candidates for OL-related applications, such as the protection of human retinal and delicate optical sensors from high-power laser radiation. These materials should exhibit high transmittance, obeying the linear Beer–Lambert law, for low incident laser intensities or fluences and a decreasing transmittance for higher incident fluences. The value of input fluence at which the transmittance begins to deviate from the Beer–Lambert regime, defined as the optical limiting onset (OL<sub>on</sub>), is usually used for the assessment of the OL efficiency of a material.

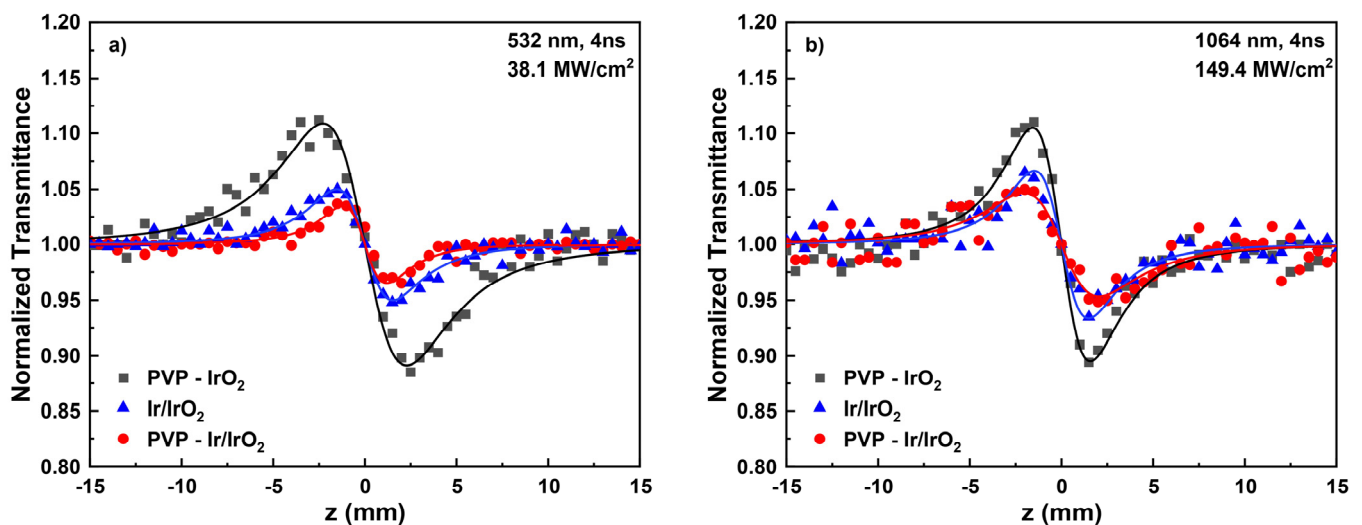
For the determination of the OL<sub>on</sub> values of the PVP-Ir/IrO<sub>2</sub> and Ir/IrO<sub>2</sub> nanohybrids, their transmittance at each laser radiation intensity was evaluated from the OA Z-scan transmittance data shown in Figure 9d,f using Equations (5) and (6). The obtained results are presented in Figure 9d,f, where, as can be seen, the OL<sub>on</sub> values of PVP-Ir/IrO<sub>2</sub> and Ir/IrO<sub>2</sub> are approximately 0.38 and 0.18 J/cm<sup>2</sup>, respectively, while their normalized transmittance drops at 78 and 75% for the highest incident laser fluence. Since ESA is the physical process responsible for the RSA behavior of the studied Ir-based nanohybrids, their OL performance can be described in terms of this mechanism.

For a more comprehensive picture of the OL efficiency of PVP-Ir/IrO<sub>2</sub> and Ir/IrO<sub>2</sub>, the determined values of  $\beta$  (or  $\text{Im}\chi^{(3)}$ ) and OL<sub>on</sub> have been compared to those of other semiconducting nanoparticles reported as efficient OL materials, such as zinc oxide (ZnO), indium zinc oxide (InZnO), titanium dioxide (TiO<sub>2</sub>), nickel oxide (NiO), chromium oxide (Cr<sub>2</sub>O<sub>3</sub>), tungsten trioxide (WO<sub>3</sub>), antimony selenide (Sb<sub>2</sub>Se<sub>3</sub>), cadmium sulfide (CdS) and silver sulfide (Ag<sub>2</sub>S) [33–38]. The results, obtained under similar excitation conditions (i.e., pulse duration and incident wavelength), are listed in Table 2. As can be seen, the present samples revealed comparable FOM and OL<sub>on</sub> values to those corresponding to other nanostructured materials included in Table 2, indicating their efficiency for OL-related applications.

**Table 2.** NLO absorption and optical limiting properties of PVP-Ir/IrO<sub>2</sub>, Ir/IrO<sub>2</sub>, ZnO, InZnO, TiO<sub>2</sub>, NiO, Cr<sub>2</sub>O<sub>3</sub>, WO<sub>3</sub>, Sb<sub>2</sub>Se<sub>3</sub>, CdS and Ag<sub>2</sub>S nanoparticles.

Sample	Excitation Conditions	$\alpha_0$ (cm <sup>-1</sup> )	$\beta$ $\times 10^{-11}$ (m/W)	$\text{Im}\chi^{(3)}$ $\times 10^{-13}$ (esu)	$\text{Im}\chi^{(3)}/\alpha_0$ $\times 10^{-13}$ (esu cm)	OL <sub>on</sub> (J/cm <sup>2</sup> )	Ref.
PVP-Ir/IrO <sub>2</sub>	4 ns, 532 nm	1.8	13.8	6.3	3.5	0.38	this work
Ir/IrO <sub>2</sub>		1.79	24.2	11.1	6.2	0.18	
ZnO		$2.7 \times 10^5$	$4.86 \times 10^{-4}$	$2.6 \times 10^{-3}$	$0.96 \times 10^{-8}$	N/A	
InZnO	6 ns, 532 nm	$1.8 \times 10^5$	$5.58 \times 10^{-4}$	$3.4 \times 10^{-3}$	$1.9 \times 10^{-8}$	N/A	[33]
TiO <sub>2</sub>	6 ns, 532 nm	~6.9	395	181.6	26.3	~1	[34]
NiO	5 ns, 532 nm	N/A	3.5–31	1.9–16.5	N/A	~0.8–1	[35]
Cr <sub>2</sub> O <sub>3</sub>	4 ns, 1064	0.31	3.17	3	9.7	~0.8	[36]
WO <sub>3</sub>		0.25	2.51	2.4	9.6	~1.9	
Sb <sub>2</sub> Se <sub>3</sub>	15 ns, 532 nm		50			2	[36]
CdS	4.1 ns, 532 nm	1.37	N/A	N/A	N/A	1.4	[38]
Ag <sub>2</sub> S		0.73	N/A	N/A	N/A	0.6	

In Figure 10, representative “Divided” Z-scans of the PVP-IrO<sub>2</sub>, PVP-Ir/IrO<sub>2</sub> and Ir/IrO<sub>2</sub> colloidal solutions prepared in methanol, obtained using 4 ns laser pulses at 532 (Figure 10a) and 1064 nm (Figure 10b), are shown. To facilitate comparisons, the measured “Divided” Z-scans correspond to solutions exhibiting a linear absorption coefficients  $\alpha_0$  of about 1.8 and 0.4 cm<sup>-1</sup> at 532 and 1064 nm, respectively. The continuous lines represent the best-fitting curve to the obtained experimental data (solid points) according to Equation (2). As can be seen, all solutions displayed a peak–valley configuration under both excitation wavelengths, denoting a self-defocusing behavior (i.e.,  $\gamma' < 0$ ). Moreover, PVP and methanol did not exhibit measurable NLO refraction under the present excitation conditions. Therefore, the nonlinear refractive index parameter  $\gamma'$  of the studied nanohybrids can be straightforwardly obtained from the “Divided” Z-scans shown in Figure 10. Consequently, from the fitting of these recordings, the nonlinear refractive index parameter  $\gamma'$  of PVP-IrO<sub>2</sub>, PVP-Ir/IrO<sub>2</sub> and Ir/IrO<sub>2</sub> were determined to be about  $(-89.8 \pm 16.0) \times 10^{-21}$ ,  $(-20.0 \pm 2.0) \times 10^{-21}$  and  $(-28.8 \pm 2.0) \times 10^{-21}$  m<sup>2</sup>/W, respectively, at 532 nm, and about  $(-28 \pm 4) \times 10^{-21}$ ,  $(-7.8 \pm 0.4) \times 10^{-21}$ ,  $(-13.3 \pm 2.0) \times 10^{-21}$  m<sup>2</sup>/W at 1064 nm. The above values demonstrate nicely that the increase in IrO<sub>2</sub> concentration results in the enhancement of the NLO refraction of the samples.

**Figure 10.** “Divided” Z-scans of PVP-IrO<sub>2</sub>, PVP-Ir/IrO<sub>2</sub>, Ir/IrO<sub>2</sub> nanohybrid solutions under (a) 532 and (b) 1064 nm laser excitation.

At this point, it is interesting to note that during ns laser excitation, free carrier refraction and thermal lensing are the most sizable contributions to the observed refractive nonlinearity. The former process is attributed to the more efficient electronic transitions that occur, while the latter is due to the increase in the thermal energy accumulated in the sample [54,55]. However, in the present case, the manifestation of thermal lensing should be excluded, since the laser repetition rate was kept at as low as 1 Hz, while measurements using higher repetition rates (i.e., up to 10 Hz) did not show significant modification of the sample's transmittance. Consequently, it can be safely concluded that free carrier refraction is the dominant mechanism contributing to the NLO refraction of the present nanohybrids.

By following the standard procedures used for the analysis of the obtained Z-scan recordings [47], the values of NLO parameters, i.e., the nonlinear absorption coefficient  $\beta$ , the nonlinear refractive index parameter  $\gamma'$  and the third-order susceptibility  $\chi^{(3)}$ , have been calculated and are summarized in Table 3. To facilitate the comparison among the samples with different absorption  $\alpha_0$ , the quantity  $\chi^{(3)}/\alpha_0$  is also included in Table 3.

**Table 3.** Determined NLO parameters of PVP-stabilized IrO<sub>2</sub> and Ir/IrO<sub>2</sub> and non-polymeric Ir/IrO<sub>2</sub> nanohybrids under 4 ns visible (532 nm) and infrared (1064 nm) laser excitation for different solution concentrations.

$\lambda$ (nm)	Samples	C (mmol/L)	$\alpha_0$ (cm <sup>-1</sup> )	$\beta$ $\times 10^{-11}$ (m/W)	$\gamma'$ $\times 10^{-18}$ (m <sup>2</sup> /W)	$\chi^{(3)}$ $\times 10^{-13}$ (esu)	$\chi^{(3)}/\alpha_0$ $\times 10^{-13}$ (esu cm)
532 nm	PVP-IrO <sub>2</sub>	4.5	1.77	-115.6 ± 18.0	-89.8 ± 16.0	113.6 ± 20.0	65.3 ± 11.0
		0.6	0.24	-18.2 ± 2.0	-11.1 ± 2.0	15.0 ± 2.0	62.5 ± 10.0
	PVP-Ir/IrO <sub>2</sub>	[Ir]: 0.9; [IrO <sub>2</sub> ]: 3.6	2.92	21.0 ± 2.0	-30.5 ± 3.0	35.6 ± 4.0	12.2 ± 1.0
		[Ir]: 0.5; [IrO <sub>2</sub> ]: 2.1	1.8	13.8 ± 2.0	-20.0 ± 2.0	23.3 ± 3.0	12.9 ± 1.0
	Ir/IrO <sub>2</sub>	[Ir]: 2.2; [IrO <sub>2</sub> ]: 2.2	3.15	47.7 ± 6.0	51.9 ± 6.0	61.4 ± 7.0	19.4 ± 2.0
		[Ir]: 1.2; [IrO <sub>2</sub> ]: 1.2	1.79	24.2 ± 2.0	-28.8 ± 2.0	34.2 ± 3.0	19.1 ± 2.0
1064 nm	PVP-IrO <sub>2</sub>	4.5	0.39	-	-28 ± 4	31.9 ± 5.0	82.9 ± 12.0
		2.5	0.22	-	-14.3 ± 1.0	16.3 ± 1.0	75.8 ± 7.0
	PVP-Ir/IrO <sub>2</sub>	[Ir]: 0.9; [IrO <sub>2</sub> ]: 3.6	0.52	-	-10.2 ± 1.0	11.3 ± 1.0	21.6 ± 2.0
		[Ir]: 0.6; [IrO <sub>2</sub> ]: 2.6	0.38	-	-7.8 ± 0.4	8.7 ± 0.4	22.6 ± 1.0
	Ir/IrO <sub>2</sub>	[Ir]: 2.2; [IrO <sub>2</sub> ]: 2.2	0.71	-	-19.8 ± 2.0	21.9 ± 3.0	30.9 ± 4.0
		[Ir]: 1.3; [IrO <sub>2</sub> ]: 1.3	0.43	-	-13.3 ± 2.0	14.7 ± 2.0	34.0 ± 4.0

From the  $\chi^{(3)}/\alpha_0$  values shown in Table 3, it is concluded that the content of IrO<sub>2</sub> nanoparticles significantly affects the NLO response of the present Ir-based nanohybrids. More specifically, the NLO response of PVP-IrO<sub>2</sub>, containing only IrO<sub>2</sub> nanoparticles, was found to be enhanced by factors of ~10 and 5 compared to PVP-Ir/IrO<sub>2</sub> and Ir/IrO<sub>2</sub>, respectively, for visible (532 nm) laser excitation and by factors of ~4 and 2.5 for infrared (1064 nm) excitation. In addition, among the solutions containing a mixture of Ir and IrO<sub>2</sub> nanoparticles, Ir/IrO<sub>2</sub> (Ir/IrO<sub>2</sub> ratio ~1) revealed ~2 and 1.5 times larger  $\chi^{(3)}/\alpha_0$  values than PVP-Ir/IrO<sub>2</sub> (Ir/IrO<sub>2</sub> ratio ~0.25) under 532 and 1064 laser excitation, respectively. Therefore, the present findings indicate that the modification of atomic content of Ir-based nanohybrids through the choice of the suitable synthesis method can be used in the tailoring of their NLO response.

In addition, PVP-IrO<sub>2</sub> revealed saturable absorption ( $\beta < 0$ ), while both PVP-Ir/IrO<sub>2</sub> and Ir/IrO<sub>2</sub> exhibited reverse saturable absorption ( $\beta > 0$ ). This sign alternation of the nonlinear absorption coefficient  $\beta$  indicates that they can be used either as saturable absorbers or optical limiters by modifying the content of IrO<sub>2</sub> nanoparticles. Concerning the NLO refraction, all the studied nanoparticles exhibited large values of  $\gamma'$  (i.e., in the order

of  $10^{-17}$  m<sup>2</sup>/W) under both excitation wavelengths, which are comparable and even larger than those of other metal and semiconducting nanoparticles (see Table S1, Supplementary Information), suggesting that they can be suitable for optical-switching applications.

#### 4. Conclusions

In summary, Ir-based nanocolloids were synthesized in methanol, in the presence and absence of PVP, by following three different synthetic procedures, affording solutions with different ratios of Ir and IrO<sub>2</sub> nanoparticles. Their NLO response and OL efficiency was investigated under 4 ns laser excitation at 532 and 1064 nm. The obtained results reveal that the choice of different synthetic strategies significantly affects the NLO properties of the Ir-based nanohybrids, especially their NLO absorption. More specifically, the nanocolloidal system containing only IrO<sub>2</sub> nanoparticles, exhibits strong saturable absorption. On the other hand, highly stable solutions containing a mixture of Ir and IrO<sub>2</sub> nanoparticles with different ratios reveal very efficient OL performance for visible laser excitation. In addition, it was found that the IrO<sub>2</sub> content of the solutions has a great impact on their NLO absorptive and refractive response, with the solutions having a higher Ir/IrO<sub>2</sub> ratio revealing larger values of nonlinear absorption coefficient  $\beta$  and nonlinear refractive index parameter. The findings of the present study demonstrate that the variation in the Ir/IrO<sub>2</sub> ratio of Ir-based nanohybrid solutions by choosing the appropriate synthetic strategy can result in at-will NLO response in view of specific photonic and optoelectronic applications.

**Supplementary Materials:** The following supporting information can be downloaded at: <https://www.mdpi.com/article/10.3390/nano13142131/s1>, Figure S1: Tauc plots of PVP-IrO<sub>2</sub> for direct optical transitions; Figure S2: TEM image of sample I (Ir/IrO<sub>2</sub>); Figure S3: UV-Vis-NIR absorption spectra of (a) PVP-IrO<sub>2</sub>, (b) PVP-Ir/IrO<sub>2</sub> and (c) Ir/IrO<sub>2</sub> nanohybrid solutions measured in different periods; Table S1: NLO refraction of PVP-IrO<sub>2</sub>, PVP-Ir/IrO<sub>2</sub>, Ir/IrO<sub>2</sub>, Au, ZnO,  $\gamma$ -Fe<sub>2</sub>O<sub>3</sub>, poly(sodium-4-styrenesulfonate) (PSS)-Cu(OH)<sub>2</sub>, PSS-Cu(OH)<sub>2</sub>/CuO and PVP/Pd nanoparticles. Reference [56] is cited in the supplementary materials.

**Author Contributions:** Conceptualization, M.S., S.C. and T.K.-C.; methodology, N.C., M.S., S.C., G.P., R.T. and A.B.; software, N.C., M.S. and S.C.; validation, N.C., M.S. and S.C.; formal analysis, N.C. and S.C.; investigation, N.C., M.S., S.C., G.P., R.T., A.B. and T.K.-C.; resources, N.C., M.S. and S.C.; data curation, N.C. and S.C.; writing—original draft preparation, M.S.; writing—review and editing, M.S., S.C. and T.K.-C.; visualization, N.C., M.S., S.C., R.T. and A.B.; supervision, S.C. and T.K.-C.; project administration, S.C. and T.K.-C.; funding acquisition, S.C. All authors have read and agreed to the published version of the manuscript.

**Funding:** For Michalis Stavrou funding was provided by the Hellenic Foundation for Research and Innovation (HFRI) under the HFRI PhD Fellowship grant (number: 83656). For Alexander Bunge and Rodica Turcu, this work was supported by the project funded by the Ministry of Research, Innovation, and Digitalisation through Programme 1—Development of the National Research and Development System; Subprogramme 1.2—Institutional Performance—Funding Projects for Excellence in RDI, Contract No. 37PFE/30.12.2021.

**Data Availability Statement:** Not applicable.

**Acknowledgments:** Michalis Stavrou acknowledges support from the Hellenic Foundation for Research and Innovation (HFRI) under the HFRI PhD Fellowship grant (number: 83656). We thank the University of Cyprus for the financial support and the Cyprus State Scholarship Foundation for supporting the PhD studies of Georgia Paparaskeva with a full scholarship.

**Conflicts of Interest:** The authors declare no conflict of interest.

#### References

1. Rodrigues, T.S.; Da Silva, A.G.M.; Camargo, P.H.C. Nanocatalysis by Noble Metal Nanoparticles: Controlled Synthesis for the Optimization and Understanding of Activities. *J. Mater. Chem. A* **2019**, *7*, 5857–5874. [[CrossRef](#)]
2. Jin, R. The Impacts of Nanotechnology on Catalysis by Precious Metal Nanoparticles. *Nanotechnol. Rev.* **2012**, *1*, 31–56. [[CrossRef](#)]
3. Krajczewski, J.; Ambroziak, R.; Kudelski, A. Formation and Selected Catalytic Properties of Ruthenium, Rhodium, Osmium and Iridium Nanoparticles. *RSC Adv.* **2022**, *12*, 2123–2144. [[CrossRef](#)]

4. Zhang, J.; Zhang, T.; Yang, J.-H. Precious Metal Nanomaterial-Modified Electrochemical Sensors for Nitrite Detection. *Ionics* **2022**, *28*, 2041–2064. [[CrossRef](#)]
5. Doria, G.; Conde, J.; Veigas, B.; Giestas, L.; Almeida, C.; Assunção, M.; Rosa, J.; Baptista, P.V. Noble Metal Nanoparticles for Biosensing Applications. *Sensors* **2012**, *12*, 1657–1687. [[CrossRef](#)]
6. Arvizo, R.R.; Bhattacharyya, S.; Kudgus, R.A.; Giri, K.; Bhattacharya, R.; Mukherjee, P. Intrinsic Therapeutic Applications of Noble Metal Nanoparticles: Past, Present and Future. *Chem. Soc. Rev.* **2012**, *41*, 2943. [[CrossRef](#)]
7. Azharuddin, M.; Zhu, G.H.; Das, D.; Ozgur, E.; Uzun, L.; Turner, A.P.F.; Patra, H.K. A Repertoire of Biomedical Applications of Noble Metal Nanoparticles. *Chem. Commun.* **2019**, *55*, 6964–6996. [[CrossRef](#)]
8. Li, N.; Ma, J.; Zhang, Y.; Zhang, L.; Jiao, T. Recent Developments in Functional Nanocomposite Photocatalysts for Wastewater Treatment: A Review. *Adv. Sustain. Syst.* **2022**, *6*, 2200106. [[CrossRef](#)]
9. Jeong, S.-H.; Choi, H.; Kim, J.Y.; Lee, T.-W. Silver-Based Nanoparticles for Surface Plasmon Resonance in Organic Optoelectronics. *Part. Part. Syst. Charact.* **2015**, *32*, 164–175. [[CrossRef](#)]
10. Wei, W.; Bai, F.; Fan, H. Oriented Gold Nanorod Arrays: Self-Assembly and Optoelectronic Applications. *Angew. Chem. Int. Ed.* **2019**, *58*, 11956–11966. [[CrossRef](#)]
11. Quinson, J. Iridium and IrOx Nanoparticles: An Overview and Review of Syntheses and Applications. *Adv. Colloid Interface Sci.* **2022**, *303*, 102643. [[CrossRef](#)]
12. Handwerk, D.R.; Shipman, P.D.; Whitehead, C.B.; Özkar, S.; Finke, R.G. Particle Size Distributions via Mechanism-Enabled Population Balance Modeling. *J. Phys. Chem. C* **2020**, *124*, 4852–4880. [[CrossRef](#)]
13. Özkar, S.; Finke, R.G. Dust Effects on Nucleation Kinetics and Nanoparticle Product Size Distributions: Illustrative Case Study of a Prototype Ir(0)<sub>n</sub> Transition-Metal Nanoparticle Formation System. *Langmuir* **2017**, *33*, 6550–6562. [[CrossRef](#)]
14. Cui, M.-L.; Chen, Y.-S.; Xie, Q.-F.; Yang, D.-P.; Han, M.-Y. Synthesis, Properties and Applications of Noble Metal Iridium Nanomaterials. *Coord. Chem. Rev.* **2019**, *387*, 450–462. [[CrossRef](#)]
15. Goel, A.; Rani, N. Effect of PVP, PVA and POLE Surfactants on the Size of Iridium Nanoparticles. *Open J. Inorg. Chem.* **2012**, *2*, 67–73. [[CrossRef](#)]
16. Mévellec, V.; Roucoux, A.; Ramirez, E.; Philippot, K.; Chaudret, B. Surfactant-Stabilized Aqueous Iridium(0) Colloidal Suspension: An Efficient Reusable Catalyst for Hydrogenation of Arenes in Biphasic Media. *Adv. Synth. Catal.* **2004**, *346*, 72–76. [[CrossRef](#)]
17. Bizzotto, F.; Quinson, J.; Zana, A.; Kirkensgaard, J.J.K.; Dworzak, A.; Oezaslan, M.; Arenz, M. Ir Nanoparticles with Ultrahigh Dispersion as Oxygen Evolution Reaction (OER) Catalysts: Synthesis and Activity Benchmarking. *Catal. Sci. Technol.* **2019**, *9*, 6345–6356. [[CrossRef](#)]
18. Quinson, J.; Kacenauskaite, L.; Schröder, J.; Simonsen, S.B.; Theil Kuhn, L.; Vosch, T.; Arenz, M. UV-Induced Syntheses of Surfactant-Free Precious Metal Nanoparticles in Alkaline Methanol and Ethanol. *Nanoscale Adv.* **2020**, *2*, 2288–2292. [[CrossRef](#)]
19. Singh, S.K.; Xu, Q. Bimetallic Nickel-Iridium Nanocatalysts for Hydrogen Generation by Decomposition of Hydrous Hydrazine. *Chem. Commun.* **2010**, *46*, 6545. [[CrossRef](#)]
20. Chen, Z.; Duan, X.; Wei, W.; Wang, S.; Ni, B.-J. Iridium-Based Nanomaterials for Electrochemical Water Splitting. *Nano Energy* **2020**, *78*, 105270. [[CrossRef](#)]
21. Schick, L.; Sanchis, R.; González-Alfaro, V.; Agouram, S.; López, J.M.; Torrente-Murciano, L.; García, T.; Solsona, B. Size-Activity Relationship of Iridium Particles Supported on Silica for the Total Oxidation of Volatile Organic Compounds (VOCs). *J. Chem. Eng.* **2019**, *366*, 100–111. [[CrossRef](#)]
22. Kurbanoglu, S.; Rivas, L.; Ozkan, S.A.; Merkoçi, A. Electrochemically Reduced Graphene and Iridium Oxide Nanoparticles for Inhibition-Based Angiotensin-Converting Enzyme Inhibitor Detection. *Biosens. Bioelectron.* **2017**, *88*, 122–129. [[CrossRef](#)]
23. Zhen, W.; Liu, Y.; Lin, L.; Bai, J.; Jia, X.; Tian, H.; Jiang, X. BSA-IrO<sub>2</sub>: Catalase-like Nanoparticles with High Photothermal Conversion Efficiency and a High X-Ray Absorption Coefficient for Anti-Inflammation and Antitumor Theranostics. *Angew. Chem. Int. Ed.* **2018**, *57*, 10309–10313. [[CrossRef](#)]
24. Ito, S.; Abe, Y.; Kawamura, M.; Kim, K.H. Electrochromic Properties of Iridium Oxide Thin Films Prepared by Reactive Sputtering in O<sub>2</sub> or H<sub>2</sub>O Atmosphere. *J. Vac. Sci. Technol. B Nanotechnol. Microelectron.* **2015**, *33*, 041204. [[CrossRef](#)]
25. Hari, M.; Mathew, S.; Nithyaja, B.; Joseph, S.A.; Nampoore, V.P.N.; Radhakrishnan, P. Saturable and Reverse Saturable Absorption in Aqueous Silver Nanoparticles at Off-Resonant Wavelength. *Opt. Quant. Electron.* **2012**, *43*, 49–58. [[CrossRef](#)]
26. Papagiannouli, I.; Aloukos, P.; Rioux, D.; Meunier, M.; Couris, S. Effect of the Composition on the Nonlinear Optical Response of Au<sub>x</sub>Ag<sub>1-x</sub> Nano-Alloys. *J. Phys. Chem. C* **2015**, *119*, 6861–6872. [[CrossRef](#)]
27. Chehrghani, A.; Torkamany, M.J. Nonlinear Optical Properties of Laser Synthesized Pt Nanoparticles: Saturable and Reverse Saturable Absorption. *Laser Phys.* **2014**, *24*, 015901. [[CrossRef](#)]
28. Papagiannouli, I.; Potamianos, D.; Krasia-Christoforou, T.; Couris, S. Third-Order Optical Nonlinearities of PVP/Pd Nanohybrids. *Opt. Mater.* **2017**, *72*, 226–232. [[CrossRef](#)]
29. Alani, I.A.M.; Ahmad, B.A.; Ahmed, M.H.M.; Latiff, A.A.; Al-Masoodi, A.H.H.; Lokman, M.Q.; Harun, S.W. Nanosecond Mode-Locked Erbium Doped Fiber Laser Based on Zinc Oxide Thin Film Saturable Absorber. *Indian J. Phys.* **2019**, *93*, 93–99. [[CrossRef](#)]
30. Wang, J.; Xie, L.; Wang, Y.; Lan, Y.; Wu, P.; Lv, J.; Zhang, G.; Miao, Z.; Cheng, G. High-Damage Vanadium Pentoxide Film Saturable Absorber for Sub-Nanosecond Nd:YAG Lasers. *Infrared Phys. Technol.* **2023**, *129*, 104580. [[CrossRef](#)]

31. Chatzikyriakos, G.; Iliopoulos, K.; Bakandritsos, A.; Couris, S. Nonlinear Optical Properties of Aqueous Dispersions of Ferromagnetic  $\gamma$ -Fe<sub>2</sub>O<sub>3</sub> Nanoparticles. *Chem. Phys. Lett.* **2010**, *493*, 314–318. [[CrossRef](#)]
32. Stavrou, M.; Papaparaskeva, G.; Stathis, A.; Stylianou, A.; Turcu, R.; Krasia-Christoforou, T.; Couris, S. Synthesis, Characterization and Nonlinear Optical Response of Polyelectrolyte-Stabilized Copper Hydroxide and Copper Oxide Colloidal Nanohybrids. *Opt. Mater.* **2021**, *119*, 111329. [[CrossRef](#)]
33. Htwe, Z.M.; Zhang, Y.-D.; Yao, C.-B.; Li, H.; Li, H.-Y.; Yuan, P. Investigation of Third Order Nonlinear Optical Properties of Undoped and Indium Doped Zinc Oxide (InZnO) Thin Films by Nanosecond Z-Scan Technique. *Opt. Mater.* **2016**, *52*, 6–13. [[CrossRef](#)]
34. Krishna Mariserla, B.M.; Alee, K.S.; Kasthuri, S.; Gawas, P.; Rao, D.N.; Nutalapati, V. Broadband Optical Power Limiting with the Decoration of TiO<sub>2</sub> Nanoparticles on Graphene Oxide. *Opt. Mater.* **2020**, *109*, 110366. [[CrossRef](#)]
35. Menon, P.S.; Kunjumon, J.; Bansal, M.; Nair, S.S.; Beryl, C.; Vinitha, G.; Maity, T.; Abraham, P.M.; Sajan, D.; Philip, R. Role of Surface Defects in the Third Order Nonlinear Optical Properties of Pristine NiO and Cr Doped NiO Nanostructures. *Ceram. Int.* **2023**, *49*, 5815–5827. [[CrossRef](#)]
36. Muller, O.; Gibot, P. Optical Limiting Properties of Templated Cr<sub>2</sub>O<sub>3</sub> and WO<sub>3</sub> Nanoparticles. *Opt. Mater.* **2019**, *95*, 109220. [[CrossRef](#)]
37. Molli, M.; Pradhan, P.; Dutta, D.; Jayaraman, A.; Bhat Kademane, A.; Muthukumar, V.S.; Kamisetti, V.; Philip, R. Study of Nonlinear Optical Absorption Properties of Sb<sub>2</sub>Se<sub>3</sub> Nanoparticles in the Nanosecond and Femtosecond Excitation Regime. *Appl. Phys. A* **2016**, *122*, 549. [[CrossRef](#)]
38. Jia, W.; Douglas, E.P.; Guo, F.; Sun, W. Optical Limiting of Semiconductor Nanoparticles for Nanosecond Laser Pulses. *Appl. Phys. Lett.* **2004**, *85*, 6326–6328. [[CrossRef](#)]
39. Peng, Q.; Juzeniene, A.; Chen, J.; Svaasand, L.O.; Warloe, T.; Giercksky, K.-E.; Moan, J. Lasers in Medicine. *Rep. Prog. Phys.* **2008**, *71*, 056701. [[CrossRef](#)]
40. Dutta Majumdar, J.; Manna, I. Laser Material Processing. *Int. Mater. Rev.* **2011**, *56*, 341–388. [[CrossRef](#)]
41. Coffey, V. High-Energy Lasers: New Advances in Defense Applications. *Opt. Photonics News* **2014**, *25*, 28–35. [[CrossRef](#)]
42. Koch, T.L.; Koren, U. Semiconductor Lasers for Coherent Optical Fiber Communications. *J. Light. Technol.* **1990**, *8*, 274–293. [[CrossRef](#)]
43. Gao, Y.; Kong, D. Nonlinear Optical Response of Noble Metal Nanoparticles. In *Laser Technology and its Applications*; Ma, Y., Ed.; IntechOpen: London, UK, 2019; ISBN 978-1-78984-917-2.
44. Olesiak-Banska, J.; Waszkielewicz, M.; Obstarczyk, P.; Samoc, M. Two-Photon Absorption and Photoluminescence of Colloidal Gold Nanoparticles and Nanoclusters. *Chem. Soc. Rev.* **2019**, *48*, 4087–4117. [[CrossRef](#)]
45. Abrinaei, F.; Molahasani, N. Effects of Mn Doping on the Structural, Linear, and Nonlinear Optical Properties of ZnO Nanoparticles. *J. Opt. Soc. Am. B* **2018**, *35*, 2015–2022. [[CrossRef](#)]
46. Koczkur, K.M.; Mourdikoudis, S.; Polavarapu, L.; Skrabalak, S.E. Polyvinylpyrrolidone (PVP) in Nanoparticle Synthesis. *Dalton Trans.* **2015**, *44*, 17883–17905. [[CrossRef](#)]
47. Sheik-bahae, M.; Said, A.A.; Van Stryland, E.W. High-Sensitivity, Single-Beam n<sub>2</sub> Measurements. *Opt. Lett.* **1989**, *14*, 955–957. [[CrossRef](#)]
48. Swierk, J.R.; Méndez-Hernández, D.D.; McCool, N.S.; Liddell, P.; Terazono, Y.; Pahk, I.; Tomlin, J.J.; Oster, N.V.; Moore, T.A.; Moore, A.L.; et al. Metal-Free Organic Sensitizers for Use in Water-Splitting Dye-Sensitized Photoelectrochemical Cells. *Proc. Natl. Acad. Sci. USA* **2015**, *112*, 1681–1686. [[CrossRef](#)]
49. Brown, A.L.; Winter, H.; Goforth, A.M.; Sahay, G.; Sun, C. Facile Synthesis of Ligand-Free Iridium Nanoparticles and Their In Vitro Biocompatibility. *Nanoscale Res. Lett.* **2018**, *13*, 208. [[CrossRef](#)]
50. Finkelstein-Shapiro, D.; Fournier, M.; Méndez-Hernández, D.D.; Guo, C.; Calatayud, M.; Moore, T.A.; Moore, A.L.; Gust, D.; Yarger, J.L. Understanding Iridium Oxide Nanoparticle Surface Sites by Their Interaction with Catechol. *Phys. Chem. Chem. Phys.* **2017**, *19*, 16151–16158. [[CrossRef](#)]
51. Böhm, D.; Beetz, M.; Schuster, M.; Peters, K.; Hufnagel, A.G.; Döblinger, M.; Böller, B.; Bein, T.; Fattakhova-Rohlfing, D. Efficient OER Catalyst with Low Ir Volume Density Obtained by Homogeneous Deposition of Iridium Oxide Nanoparticles on Macroporous Antimony-Doped Tin Oxide Support. *Adv. Funct. Mater.* **2020**, *30*, 1906670. [[CrossRef](#)]
52. Lee, H.; Kim, J.Y.; Lee, S.Y.; Hong, J.A.; Kim, N.; Baik, J.; Hwang, Y.J. Comparative Study of Catalytic Activities among Transition Metal-Doped IrO<sub>2</sub> Nanoparticles. *Sci. Rep.* **2018**, *8*, 16777. [[CrossRef](#)] [[PubMed](#)]
53. Christodoulides, D.N.; Khoo, I.C.; Salamo, G.J.; Stegeman, G.I.; Van Stryland, E.W. Nonlinear Refraction and Absorption: Mechanisms and Magnitudes. *Adv. Opt. Photonics* **2010**, *2*, 60–200. [[CrossRef](#)]
54. Sutherland, R.L.; McLean, D.G.; Kirkpatrick, S. *Handbook of Nonlinear Optics*; Marcel Dekker, Inc.: New York, NY, USA, 2003.
55. Said, A.A.; Sheik-Bahae, M.; Hagan, D.J.; Wei, T.H.; Wang, J.; Young, J.; Van Stryland, E.W. Determination of Bound-Electronic and Free-Carrier Nonlinearities in ZnSe, GaAs, CdTe, and ZnTe. *J. Opt. Soc. Am. B* **1992**, *9*, 405–414. [[CrossRef](#)]
56. Tauc, J. Optical Properties and Electronic Structure of Amorphous Ge and Si. *Mater. Res. Bull.* **1968**, *3*, 37–46. [[CrossRef](#)]

**Disclaimer/Publisher's Note:** The statements, opinions and data contained in all publications are solely those of the individual author(s) and contributor(s) and not of MDPI and/or the editor(s). MDPI and/or the editor(s) disclaim responsibility for any injury to people or property resulting from any ideas, methods, instructions or products referred to in the content.